SMITH, ANNA GRAY, M.S. The Incidence of Separation Events of *Saccharomyces cerevisiae* in a Flow Displacement Chamber: Examining Shear Forces Overcoming Flo11p Mediated Adhesion to an Inert Substrate. (2018)
Directed by Drs. Amy Adamson and Dennis LaJeunesse. 46 pp.

Biofilms are present on surfaces that are exposed to a consistently aqueous environment and can be deleterious to human health. Fungal biofilm infections are a common problem in medical in-dwellings, specifically urinary catheters that need to remain in the patient for significant periods of time. I designed and built a flow-chamber that can be visualized with brightfield microscopy to confirm adhesion of *Saccharomyces cerevisiae* to an inert substrate. I then used a peristaltic pump to propagate an up-stepping flow-rate and counted the number of separation events for three strains of *S. cerevisiae*, one of which is a Flo11p, *flo11Δ,* knockout. Using this flow chamber, I created adhesion profiles of *S. cerevisiae* and determined what shear forces would impede the continued adherence of *S. cerevisiae* to an inert surface. By analyzing the processes involved in the initial step in biofilm formation, deposition and adhesion, we can make advances in designing surfaces to prevent and inhibit biofilm growth in medical in-dwellings and catheters.

THE INCIDENCE OF SEPARATION EVENTS OF *SACCHAROMYCES CEREVISIAE* IN A FLOW DISPLACEMENT CHAMBER: EXAMINING SHEAR FORCES OVERCOMING Flo11p MEDIATED ADHESION TO AN INERT SUBSTRATE

by

Anna Gray Smith

A Thesis Submitted to
the Faculty of The Graduate School at
The University of North Carolina at Greensboro
in Partial Fulfillment
of the Requirements for the Degree
Master of Science

Greensboro
2018

Approved by

_____
Committee Co-Chair

_____
Committee Co-Chair

APPROVAL PAGE

This thesis written by Anna Gray Smith has been approved by the following committee of the Faculty of The Graduate School at The University of North Carolina at Greensboro.

Committee Co-Chair _____

Committee Co-Chair _____

Committee Members _____

_____

_____
Date of Acceptance by Committee

_____
Date of Final Oral Examination

ACKNOWLEDGEMENTS

I would like to thank Drs. Amy Adamson and Dennis LaJeunesse for their direction and efforts in helping me to conduct this work and write this document. I would also like to thank Dr. Paul Steimle and Dr. Robert Cannon for their time and invaluable insight. I must also thank the rest of the UNCG Biology Department for their constant support, especially Meg Horton, Ann Somers, Joseph Ramos and Dr. David Battigelli.

I must also thank my family and friends for their unending encouragement. Finally, I must thank my mother, Pamela Anne Beamon; although she exists not on this physical plane, her faith and nurturing spurred me to take this next step forward.

TABLE OF CONTENTS

Page

LIST OF FIGURES

Page

CHAPTER I

INTRODUCTION

Microbial Adhesions & Biofilms

There are many different factors that determine how and why bacteria and fungi move through their environment and ultimately select which surface they will deposit on and adhere to. These factors are a complex mix of physical forces and biological determinants, from gravity to food availability (Young, 2006). As such it is commonly accepted that bacteria and other microbes thrive on a myriad of surfaces that we encounter in our everyday world; for the most part, we co-exist peacefully and without issue. Nathan's article in *Science* examines a classical view of microbial pathogenicity and counters with a context dependent view of pathogenicity, which no longer assumes that certain microbes are simply non-pathogenic. Nathan assumes that any microbe can be pathogenic; it is merely dependent on contextual clues from its environment, the host's immune system, or its acquisition of virulence factors (Nathan, 2015). This casts the studies of microbes, their deposition and adhesion onto surfaces, and development into biofilms an especially important topic for the health and wellbeing of modern humans.

Garrett et al. highlights several deleterious situations to human health based on bacterial and fungal adhesion to surfaces within the home, industrial, and medical settings. These situations range from intestinal distresses from the home and food industries to biofilm formations on medical and dental tools and fluid lines. Garrett et al. also notes that biofilm formation is present on a great variety of surfaces that are exposed to a consistently aqueous

environment (Busscher, 2006) and the mechanics of biofilm formation are well understood (Young, 2006) (Garret, 2008) (Busscher, 2006).

The process of biofilm formation begins with the deposition of microbial cells, both bacterial and fungal, that move freely in an aqueous solution through their own locomotive processes, (flagella, etc.) or via natural physical and chemical processes (Brownian motion, gravity, chemotaxis, etc.) onto a surface (Young, 2006) (Garret, 2008). Once there, a certain portion of cells undergo a reversible adhesion while a certain other portion of these cells undergo an irreversible adsorption and adhere to the surface substrate via physical means (Garret, 2008) that will be discussed in detail below. Once these irreversibly adsorbed cells are stationary, they then divide and further populate the biofilm with daughter cells. After the initial growth phase of these stationary cells, the physical and chemical processes dominating the attachment and adsorption to the surface become overwhelmed by biological processes (extrusion of biopolymers and cohesive forces between cells) that now determine attachment both to the surface substrate and to other cells (Garret, 2008) (Busscher, 2006).

Adhesion is defined as when a cell that has been moving through in the environment in an unbound state attaches to a surface with a reversible attachment at first and then switches to an irreversible attachment (Hermansson, 1999). The physical forces involved in the adhesion processes of free moving cells within an aqueous environment to a surface are both attractive and repulsive and have been classically described by Derjaguin—Landau—Verwey—Overbeek (DLVO) theory (Hermansson, 1999). The advantages of this theory are that it can address these forces in both a qualitative and quantitative manner. The basic tenet of DLVO theory is that the net interaction (V_{Tot}) between a microbial cell and the substrate of interest is the sum of the attractive van der Waals forces (V_A) and the repulsive interactions (V_R) from the electrical double layer of the cell and the substrate.

$V_{TOT} = V_A + V_R$, V_A is defined as:

$V_A = - Ar/6d$, where A is the Hamaker constant, d is the separation distance between the cell and the substrate and r is the radius of the cell interacting with the substrate. The Hamaker constant is a property of the material in question that defines the quality of the interaction between the surface and the medium, and Hermansson tells us that the Hamaker constant is usually positive for surfaces in an aqueous medium. As the radius, r, of the contacting region between the cell and the surface of the substrate becomes smaller the total adhesion interaction is lowered and adhesion is facilitated. Distance between the cell and the surface of the substrate is dependent on the nature of the surface molecules of the cell in questions. Obviously, extrusions of proteins and oligosaccharides from the cell membrane decrease the discrete distance between the cell and the substrate surface and with a decreasing distance V_A becomes larger and overcomes the repulsive effects of V_R such that adhesion is facilitated (Hermansson, 1999).

While DLVO theory lends us an appropriate tool for approximating the forces facilitating adhesion, it unfortunately does not include a complete summation of the physical interactions in the process of adhesion between a cell and a substrate surface. It assumes perfectly smooth substrate surfaces and also does not take into account surface hydrophobicity of the cells or the abiotic surface to which the cells are adhering. Thus, modification of the DLVO theory to an 'extended' version that includes hydrophobic/hydrophilic interactions and osmotic interactions has been developed. The 'extended' DLVO theory is as such:

$\Delta G^{adh} = \Delta G^{vdW} + \Delta G^{dl} + \Delta G^{AB}$, where ΔG^{vdW} represents the attractive van der Waals forces and ΔG^{dl} represents the repulsive electric double layer forces. ΔG^{AB} is the component that describes the attractive hydrophobic interactions and the repulsive hydration effects which have been documented to be many times stronger than the van der Waals forces at play in the system.

This extended theory generally provides a better approximation of the adhesion results than classical DLVO theory, but Hermansson also cites a previous paper that comes to the conclusion that the likelihood that a theory that will fully explain microbial adhesion to latent surfaces is unlikely and such a theory will probably never be achieved (Hermansson, 1999). Understanding DLVO theory helps to build a foundation of the physical and chemical forces at play in microbial adhesion as the first step in the process of biofilm formation.

Biofilms in Urological Catheters

The urethral anatomy and environment while catheterize is a prime environment for the formation of biofilms (Farrag, 2015)((Mohammadi, 2012). The urethra in males is approximately 17.5 to 20 cm long (Standring, 2008) and can be divided into several different segments with varying calibers (Tailly, 2016). In females, the urethra is 4 cm and can also be divided into several segments with a less varied caliber along its length due to the absence of reproductive organs along the urethra that are present in males (Tailly, 2016). The lumen of the urethra has an epithelial lining and several glands which produce a lubrication on the surface of the epithelium to facilitate the passage of urine along the urethra and out of the body (Garner, 2006).

Sometimes it is necessary to catheterize a patient to facilitate the passage of urine from the body. There are many different variations of the types and materials of catheters used and catheterization of males is decidedly more complex than that of females due to the extra length and varying caliber of the urethra (Tailly, 2016). Current catheterization practices elucidates two ways microbial organisms can cause catheter associated urinary tract infections: extraluminal and intraluminal. The introduction of organisms via the extraluminal route occurs when the commensal perineal organisms are collected on the surface of the catheter during insertion or

after insertion when the perineal organisms gather and migrate along the surface of the catheter to the interior of the body. Intraluminal infection occurs when contaminated urine (either previously contaminated or from a break in the urine collection system occurs allowing organisms to infiltrate the closed, previously sterile system) refluxes back into the bladder (Siddiq, 2012).

While the majority of catheter associated urinary tract infections are bacterial, Mohammadi found out of the 55 catheters collected in their survey, 29% of infecting organisms were yeast; all of the yeast species identified were all of the Candida genus (Mohammadi, 2012). Farrag found that out of 100 patients, there were 23 isolates of yeast identified which came from several different genera (including *Candida* and *Saccharomyces*.) Thus, while medical practitioners may focus on the more prevalent bacterial catheter associated urinary tract infections, there is a medical need to develop strategies to prevent yeast biofilm formation as well. Most of the recommendations made by Hooton in the *International Clinical Guidelines* are procedural and would aid the prevention of bacterial as well mycotic catheter associated urinary tract infections and biofilm formations (Hooton, 2010). These guidelines vary, but specifically recommend intermittent and condom catherization to prevent long-term indwelling catherization due to the frequency of catheter associated urinary tract infections (Hooton, 2010).

Medical device manufacturers are now manufacturing catheters out of different materials in the hopes of preventing inflammatory reactions, urinary tract infections and the formation of biofilms (Tailly, 2016) (Siddiq, 2012). While impregnation of the catheters with antibiotics and antimicrobial materials garnered early attention, it has been found that neither of these strategies are recommended for long term indwelling catherization (Hooton, 2010) (Siddiq, 2012). There is an obvious need for the development of catheters and other medical in-dwellings to be inherently microbicidal and prevent microbial deposition and adhesion to the surface.

Microbicidal Surfaces

Biofilm formation on surfaces presents a myriad of public health issues (Garret, 2008) and much work has been done in the design and manufacture of antimicrobial surfaces (Ivanova E. P., 2012). Ivanonova et al saw upon examination of cicada (*Psaltoda claripennis*) wings that they were naturally bactericidal against the gram-negative bacteria, *Pseudomonas aeruginosa*. They acknowledge that this discovery was novel. While the wings are themselves surperhydrophobic, the surface chemistry was not the limiting factor. In fact, the rupture and death of the bacterial cells on the cicada wing was attributed to physio-mechanical forces from the wing surface structure (Ivanova E. P., 2012) (Pogodin, 2013). The wing surfaces did not prevent adhesion of the cells onto the surface but cell death occurred quite rapidly after the cells adhered to the wing surface (Ivanova E. P., 2012). The Cicada wing surfaces are covered in conical nanopillars approximately 200 nm tall and spaced approximately 170 nm apart, from center to center. It was determined that the cause of the rapid cell death is due to rupturing of the bacterial cell membrane attributed to non-uniform stretching of the membrane from adhesion to the nanopillars. The logic is as follows: the surface area of the membrane that adsorbs to the surface of the pillars expands quite rapidly and the region of the membrane that is stretched between the pillars is stretched too rapidly and ruptures. This rapid and widespread membrane rupture between the pillars causes cell death (Pogodin, 2013). Other insect wings (dragonfly, *Diplacodes bipunctata*) were also bactericidal and efficient in causing cell death in both gram-negative species (*Pseudomonas aeruginosa*) and gram-positive species (*Staphylococcus aureus* and *Bacillus subtilis*) (Ivanova E. P., 2013). (Cicada wings were found to have effective bactericidal activity in gram negative species only. Gram-positive bacteria have a more rigid cell-wall that resists stretching forces more readily than gram-negative species (Pogodin, 2013).)

This discovery has driven the search for synthetic nanostructured surfaces that can be manufactured to exact specifications with this physio-mechanical microbicidal activity. Experiments with ion-etched black silicon show similar results to that of the dragonfly (*D. bipunctata*) wing in its ability to cause cell death in both gram-negative and gram-positive bacteria (Ivanova E. P., 2013). Previous work by our lab (Nowlin, 2015) has shown that manufactured nanostructured surfaces with similar specific pillar geometry cause cell death in a eukaryotic organism, *Saccharomyces cerevisiae*, similar in magnitude to what has been previously seen with gram-negative and gram-positive prokaryotes. Experimental evidence suggests a departure from the physio-mechanical forces being solely responsible for cell rupture and includes the hypothesis that adhesion proclivities of the yeast to the surface substrate (through extended DLVO theory and attractive hydrophilic interactions between the surface substrate and the cell surface) is in part responsible for mitigating cell death (Nowlin, 2015). While we often consider both bacteria and yeast to be both pathogenic, it is important to note how the differences in cell morphology affect adhesion to latent surfaces. Young brings attention to the profound effect that bacterial shape has on mitigating adhesion in flow systems with shear forces acting on the cells. These cells, because they lack a rigid cell wall, can more easily adapt to an environment of constantly changing flow rates by changing morphology and exposing greater surface area to the shear forces to enhance and facilitate adhesion to the surface (Young, 2006). Consequently, we can assume that yeast cannot respond in a similar manner due to increased rigidity afforded via components of their cell wall and must compensate with increased reliance on adhesion proteins, one of which is of particular importance, Flo11p (Vachova, 2011).

Flo11p Protein

The *Saccharomyces cerevisiae* cell wall regulates osmotic balance within the cell by protecting the cell from drastic environmental changes while also maintaining a basic cell shape;

it is both elastic and strong and can protect the cell against shear forces (Levin, 2011). The cell wall is comprised of two layers each with specific functionality; the inner layer is sandwiched between two outer layers. The inner layer, which is responsible for the elasticity and strength of the cell wall is comprised of glucan polymers, β-1, 3-glucan chains, and chitin (Levin, 2011) (Kollar, 1997). The outer layer is composed of two classes of glycoproteins: glycosylphosphatidylinositol (GPI) proteins that have a lipid anchor in the plasma membrane at their C terminus which is then cleaved once they are fully secreted from the cell and Pir proteins which connect and cross-link to the β-1, 3-glucan chains at multiple sites (Levin, 2011) and thus provides the structural support the cell wall requires (Kollar, 1997) (Vachova, 2011).

Flo11p is a surface mannoprotein in the *Saccharomyces cerevisiae* cell wall that is integral to the formation of biofilms and the adherence of the cell to latent substrates (Vachova, 2011) (Douglas, 2007). It is also a member of the adhesins family of cell surface proteins, which are indicated in the adherence of yeast from *Candida* genera to host tissues and cause fungal pathogenicity (Douglas, 2007) (Vachova, 2011). Flo11p clusters on the surfaces of the cell and has an N-terminal A domain, which is distinctly different in its structure from the other Flo proteins that mediate cell-cell interactions and adhesions. Several studies have indicated that the hydrophobicity of the Flo11p protein mediates and initiates the initial adhesion to latent surfaces (Reynolds, 2001) (Vachova, 2011) (Kraushaar, 2015) with a fibronectin type-III-like domain in the A domain, which has two anti-parallel β sheets that are responsible for the adhesion of the protein to the latent surface (Kraushaar, 2015).

For our studies, our laboratory was generously gifted a Flo11p, *flo11Δ,* knockout strain, TBR5, of *Saccharomyces cerevisiae* from Todd Reynolds at the University of Tennessee at Knoxville. The strain was created by replacing the Flo11p reading frame with a kanamycin

resistance gene (Reynolds, 2001). He also gifted us the parent wildtype strain, TBR1, which we used as a basis for comparison.

Shear Forces in Flow Displacement Systems

Some of the previously described microbicidal surface experiments have been representative of static experiments; the environment and the cellular material attaching to the substrate remain still and unmoving. Unfortunately, biofilm formation does not always occur in such an easily controlled experimental environment. Biofilm formation is especially implicated in fluid systems (Busscher, 2006). In these fluid systems, bacteria and other pathogens are constantly buffeted by a variable or constant flow of liquid and adhesion in these systems can be affected greatly by the changes in fluid velocity (Young, 2006) and flow rate (Busscher, 2006). The dimensions of the flow system are important as well. Flow rate increases with distance away from the substrate surface and thus the forces at the apex of the cell are greater than the forces at the surface where the base of the cell sits, which generates a shear. This shear force acts parallel to the substrate surface and is dependent on the viscosity of the fluid and the dimensions of the cell (Busscher, 2006). Mathematically we can define shear force as:

$\tau = F/A = \eta\sigma$, where η is the shear stress, F the force, A the area on which the force is exerted, η the absolute viscosity and σ the shear rate. σ can then be defined as:

$\sigma = 3Q/2b^2 w$, where Q is the flow rate, b being the half depth of the chamber/displacement system and w being the width. Determining the shear force on a single cell τ_{cell} then becomes:

$\tau_{cell} = \sigma \times A_{cell}$, where A_{cell} is the surface area exposed to the shear (Nejadnik, 2008.).

The determination of these shear forces is important in determining whether an initial adhesion event will occur. Studies have shown that adhesion is both positively and negatively influenced by increases in shear stress. Lecuyer describes previous experiments done with *Escherichia coli* in which increases in shear stress increase adhesion events on specially designed surfaces due to catch-bonds between mannose surface molecules and proteins in the bacterial cell wall. Their work on *Pseudomonas aeruginosa* finds that adhesion increases as shear stress increases on glass and PMDS (polydimethylsiloxane), which has a hydrophobic surface substrate. This might indicate that adhesion in flow displacement systems on abiotic surfaces are non-surface specific and is due to other biological factors at play from the stresses of the forces within the system (physical changes in cell shape and biological modifications of the substrate surface from the cells (Lecuyer, 2011)).

CHAPTER II

SPECIFIC AIMS AND HYPOTHESES

Aim 1

Can I design and manufacture a flow chamber system that will allow us to analyze the number of separation events of *Saccharomyces cerevisiae*?

a) Find a suitable material for a flow chamber that will adapt to several different design specifications with plain glass as the substrate.
b) Validate the proof of concept flow chamber system by visualization of the separation events of *Saccharomyces cerevisiae*, using brightfield imaging.
c) Optimize flow-rate conditions to create a baseline separation profile for the wildtype strain, SK1, of *Saccharomyces cerevisiae*. Creating this separation profile will set a baseline for further studies of the flow chamber system that will allow us to accurately characterize the conditions in which shear forces overwhelm the adhesive and adsorptive abilities of the yeast to a plain glass substrate.

Hypothesis: I should be able to design and build a flow displacement chamber that allows sufficient imaging of the initial adhesion of *Saccharomyces cerevisiae* to the latent surface. Using this technology, I should also be able to sufficiently image and establish a separation profile of the separation events of the SK1 strain.

Aim 2

Will a Flo11 knockout, *flo11Δ,* mutant strain of yeast have increased separation events compared its parental wildtype strain using a flow chamber on plain glass?

a) Use the flow chamber to characterize the separation events in the Flo11 knockout, *flo11Δ,* yeast strain *Saccharomyces cerevisiae*, TBR5, by brightfield imaging and counting the separation events. Using the image analysis methods established in Aim 1, establish a separation profile for the TBR5 strain.
b) Use the flow chamber to characterize the separation events in the parental wildtype yeast strain S*accharomyces cerevisiae*, TBR1, by brightfield imaging and counting the separation events. Using the image analysis methods established in Aim 1, establish a separation profile for the TBR1 strain.
c) Analyze counts data within each experiment and compare separation profiles to one another via statistical methods.

Hypothesis: The Flo11p knockout yeast strain, TBR5, will have increased separation events compared to its parental wildtype strain, TBR1, on a plain glass surface when subjected to the same shear forces in a flow chamber. Comparison of the separation profiles of both of the TBR strains of yeast to one another will show that the wildtype strain, TBR1 with an intact Flo11p gene, will adhere more strongly and have fewer separation events than compared to the TBR5 strain which has no Flo11p protein.

CHAPTER III

METHODS

Experimental Design

While the majority of the data in the literature review indicate species from the *Candida* genus as the most biologically and pathologically relevant for biofilm formation within long-term indwelling catheter, there is some evidence that yeast of the *Saccharomyces* genus can cause catheter associated urinary tract infections. (Farrag, 2015) For our experiments, I chose to work with *Saccharomyces cerevisiae* because of its relatively low pathogenicity (BSL1), ease of genetic manipulation, and easily demonstrable model of adhesion to latent surfaces (Reynolds, 2001) (Vachova, 2011) (Kraushaar, 2015). The Flo11p protein is also related to the Als adhesin protein in *Candida* species (Vachova, 2011) (Ramsook, 2010). The data that I collect in these studies with *Saccharomyces cerevisiae* can be used to lay the groundwork for future studies with *Candida* species.

Design of the Flow Chamber

Several considerations were taken into account in the design of flow chamber. It needed to be easily manufactured, relatively cheap and accommodate different, specific design specifications. Many labs are using PDMS (Polydimethylsiloxane) to develop microfluidic devices (Kang, 2017) (Shrirao, 2010). PDMS is an ideal substrate to develop a flow chamber in that is not cost-prohibitive and is transparent. It initially is a liquid and can readily accommodate many different design specifications. I had previously contemplated 3D printing a flow chamber, but this is an expensive and lengthy process. The size of the imaging lumen was a limiting factor

as well, the 3D printer available to us could not accommodate such a small dimension; thus, I decided to proceed with manufacturing flow chambers with PDMS.

The dimensions of the flow chamber were limited by the size of the coverslips that the chamber would be placed on. The confocal microscope used for imaging is an inverted scope and thus the imaging thickness of the glass was limited to the thickness of a coverslip. Ted Pella Inc. manufactures coverslips that are 3x3.5 inches. I determined that this would give us adequate room for the tubing input channel, the imaging lumen, and an exit channel for the waste fluid. I was able to 3D print the shell for the flow chamber mold. I made two depressions on the two shorter sides of the bottom of the shell to accommodate the capillary tubes. The capillary tubes were of similar diameter of the tubing of from the peristaltic pump so they served as the mold for the input and exit channels for the tubing and the fluid in the flow chamber.

The imaging lumen of the flow chamber needed to be of adequate imaging length and also lengthy enough to establish a laminar flow and propagate the established flow rate velocity. The imaging lumen also needed to provide an adequate imaging surface area that is free of obstruction from PDMS. After several attempts with a round, 18-gauge wire I determined that the imaging area (the area where the wire is in contact with the glass during manufacture) was not sufficient for imaging, thus I decided to proceed with a square 18-gauge wire since it had a significantly larger surface area where it came into contact with the glass. With the design limitations considered and met, I was able to move forward to manufacturing the flow chambers.

Manufacture of the Flow Chamber

Before manufacturing the flow chamber, a piece of 5x7 inch glass was cleaned and prepped. Nitrile gloves were worn at all times during the handling of the glass to prevent any skin oil deposit on the surface of the glass. Any residue from a previous flow chamber was

removed from the surface of the glass by scraping the surface with the beveled edge of a razorblade. Once the previous residue had been removed the glass was soaked in hot tap water and Fisherbrand Sparkleen for 5 minutes. The glass was then hand agitated in the Sparkleen for an equal amount of time followed by rinsing in copious amounts of hot tap water. Once all the detergent was rinsed from the surface of the glass, it was set to cool at room temperature. After the glass cooled to room temperature, it was rinsed in copious amounts of room temperature distilled water. If any residues on the surface of the glass or perturbations in the flow of distilled water over the surface of the glass were observed during the distilled water rinse, the previous scraping and cleaning procedure was repeated. Once the surface of the glass was observed to be residue and perturbation free, the glass was then rinsed in copious amounts of 95% Ethanol (EtOH) to evaporate any remaining water from the surface. To completely dry the glass, the glass was held under a jet-air stream within a fume hood and all liquid was pushed off the surface. After the surface was completely dry, the glass was ready for the manufacture of the flow chamber.

The glass to which the PDMS flow chamber was poured was handled only by the edges wearing nitrile gloves to avoid contaminating the surface with skin oils. A one-inch long segment of the 18-gauge square wire was obtained and laid on the glass surface with a pair of metal forceps ensuring that a flat edge of the wire was in complete contact with the surface of the glass. Two Fisherbrand capillary tubes were obtained and placed on either end of the 18-gauge wire with the edges of the one end of the capillary tube abutting the edge of the wire. A layer of Vaseline was applied to the bottom, flat surface of the pre-printed 3D shell using a gloved finger. Enough Vaseline was applied to achieve complete coverage of the bottom surface and in the depressions for the capillary tubes. The 3D printed shell was then inverted and gently placed onto the glass with the depressions in the printed shell lining up with the capillary tubes. The 3D

printed shell was gently pressed down until the Vaseline secured the shell to the glass plate. Once the flow chamber mold set-up was complete as in Figure 1 below, the PDMS needed to be prepared.

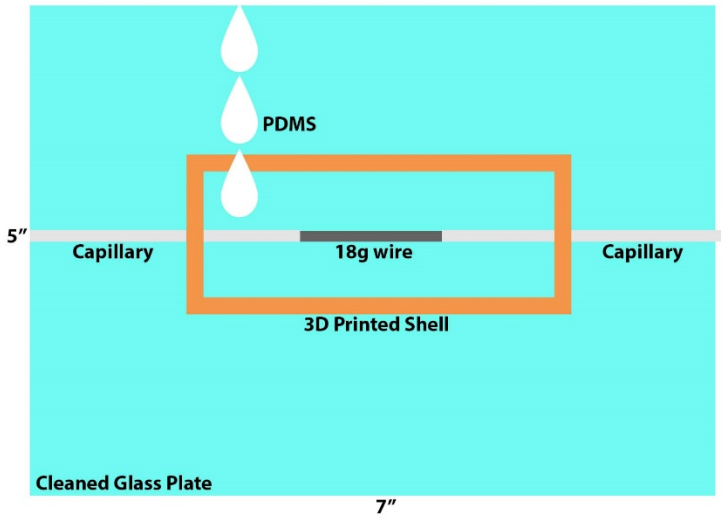

Figure 1. Schematic of Flow Chamber Mold Set-Up

The PDMS was prepared by mixing the contents of the large jar, Part A, to the contents of the smaller jar, Part B, at a 10:1 weight/weight ratio. The two parts were weighed and then Part B was poured into the container with Part A and mixed vigorously with a metal scooper. Once the two parts were mixed thoroughly, indicated by the presence of many bubbles, the mixed PDMS was poured into the interior of the 3D printed shell as indicated by Figure 1. PDMS is a fairly viscous liquid and often would not immediately spread to evenly fill the mold. If the PDMS was not filling in the mold evenly, the glass was gently agitated back and forth to facilitate the PDMS evenly filling the 3D printed shell. Once the shell was filled with PDMS, the glass was carefully placed into a 65°C oven for 1 hour to remove the bubbles from the flow chamber. After one hour, the glass was removed from the oven and then left to sit at room temperature overnight to let the flow chamber finish curing.

After the flow chamber was finished curing, any excess PDMS was cut away from the exterior of the 3D printed shell and the capillary tubes using a razor blade. The razor blade was used to score the PDMS on the inside border of the shell as well. The 3D printed shell was then pried away from the glass using the razor blade to go around each face of the shell. Once the shell was separated from the glass, it was pulled vertically off the flow chamber. The flow chamber was removed from the surface of the glass by using the razor blade to lever each face slightly off, moving in a clockwise motion around the mold repeatedly until it released from the surface of the glass. On some occasions the capillary tubes and the 18g wire were also removed from the surface of the glass and remained in the PDMS mold. On these occasions the razor blade was used to gently prize the wire and the capillary tubes out of the PDMS. Any thin sheets of PDMS that were occluding the imaging area where the 18g wire was were removed either with sharp metal forceps or the razor blade.

After a few attempts at this design (capillary tube, 18g wire, capillary tube), it was discovered that there was often a thin sheet of PDMS that was occluding the opening where the 18g wire and the capillary tubes met in the mold. The design was altered such that a length of 18g square wire was ran the entire length of the channel; it is a similar size of the tubing as well and adequately accommodated it at testing. At the completion of these steps the flow chamber was ready for experimentation.

Yeast Culturing

The yeast strains were grown by seeding 10mLs of YPD (Yeast Extract – 20%, Peptone – 10%, Dextrose – 20%) media with 1 colony from a pre-streaked plate and grown overnight to an OD600 of around 1.5. In the morning, fresh cultures were spiked with the cells from the

overnight culture to an OD600 of 0.2 and grown until OD600 of 0.4 – 0.6. This was done to ensure that the cells were in the growth phase and had not entered the stationary phase.

The cells were then laid onto the coverslip in a line down the center of the coverslip and allowed to adhere to the coverslip for 30 minutes at room temperature. Before placing the flow chamber onto the coverslip for imaging, the flow chamber was cleaned in the plasma cleaner to rid the surfaces of any debris and create a better adhesion of the flow chamber to the coverslip. The coverslips were also previously cleaned in Nitric and Hydrochloric Acid for 30 mins and then rinsed with copious amounts of distilled water until the pH of the water rinse was equal to the house supply of distilled water. The coverslips were then soaked in distilled water for 30 minutes and then removed from the water. Any excess water was wicked off the surface. The coverslips were then sealed in a glass petri dish for future use.

After cleaning and the 30-minute adherence incubation, the flow chamber was seated onto the center of the coverslip and loaded onto the microscope slide holder for imaging. A 1X PBS solution was loaded into the syringe feeding the pump and the input tubing was connected to the input side of the flow chamber and the waste tubing was connected to the opposite side of the flow chamber for waste solution collection.

Imaging

Image acquisition was done with a Zeiss Axio Spinning Disk Confocal Fluorescence Microscope. The imaging area was found and centered using transmitted light; all imaging was done using brightfield imaging. Figure 2, shows a standard imaging set-up of the flow chamber on the microscope. The Harvard Apparatus Peristaltic Pump was pre-programmed with the specific flow rate over eight minutes and started. The microscope imaging software was pre-programmed to take a brightfield image every fifteen seconds over the same time duration as the

pump was pumping. I established a step-up flow rate with the following profile: $5^{\mu l}/_{minute}$ for T_{zero} to 2 minutes, $10^{\mu l}/_{minute}$ from 2 minutes to 4 minutes, $50^{\mu l}/_{minute}$ for 4 minutes to 6 minutes, and $100^{\mu l}/_{minute}$ from 6 minutes to 8 minutes. At the end of each experimental run, the images for each timepoint were then saved individually, exported into jpeg files for analysis, and compressed together into a movie for presentation.

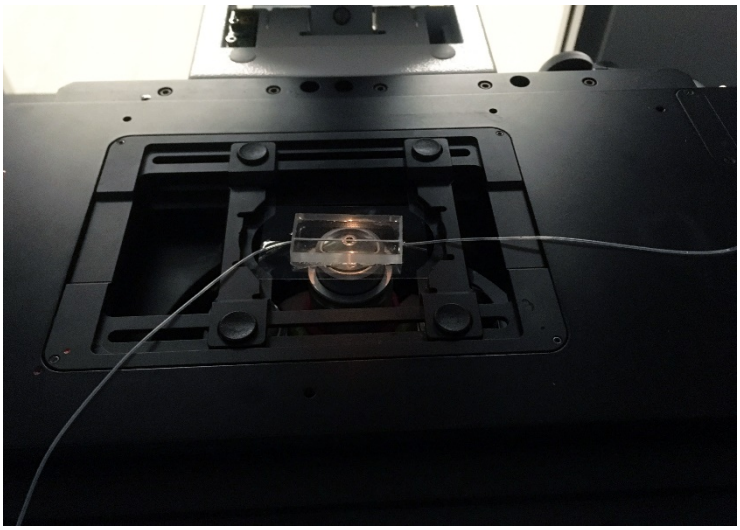

Figure 2. Imaging Set-Up on the Zeiss Axio Spinning Disc Confocal Fluorescence Microscope. The PDMS flow chamber is centered over the imaging objective. The input tubing from the peristaltic pump is coming into the chamber from the right and the waste tubing is exiting the chamber to the left. The flow chamber is loaded onto the coverslip and the setup is ready for imaging.

Image Manipulation for Analysis

To analyze the number of separation events, the number of cells adhered to the plain glass surface at time point zero were counted via a counting module in ImageJ, an imaging software publicly available from the National Institutes of Health. To determine the difference from the images representing the remaining time points to the original time point, T_{zero}, the second image was subtracted from the T_{zero} image and then the number of cells on the resulting image of the difference were counted.

To count the number of cells in each image and subtract the images from one another, there must be some image manipulation done for the commands in ImageJ. These steps are represented by Figure 3. First, the T_{zero} image was opened, see Figure 3A, and the background was subtracted, using Process -> Subtract Background. A rolling ball radius of 8.0 pixels was used for every image analyzed in these experiments. Once the background was subtracted, the Threshold menu was opened (Ctrl + Shift + T) to set what pixels would be included in the analysis. The value was set for all of the images in one experimental run using the T_{zero} image. The principal of setting an accurate threshold is to be sure that all of the pixels on the image that are representative of actual data are included but any random pixel noise is eliminated. Once the pixels values are adequate, it was set using the Apply function in the Threshold pop-up window. The image then needed to be converted to a binary image, see Figure 3B, setting all pixel values at either 0 (black) or 255 (white); this is because the selected algorithms cannot analyze shades of gray. This was accomplished via Process -> Binary -> Convert to Mask. Once the image was binary, a few more image manipulations were done. Any large areas of pixels that had touching borders and had merged into more than one cell were separated using the Process -> Binary -> Watershed command. This asks ImageJ to set borders where it assumes that there is more than one cell in a clump of cells. While this is most certainly not a perfect technique, by using the

same threshold and binary conversion for each image in an experimental run it can be assumed that ImageJ will be equally imperfect for the same cluster of pixels for each image and thus can accept the criteria it proposes for cell borders. Once the pixel clusters were separated, I asked ImageJ to fill any apparent holes in what it would assume to be one cell by Process -> Binary -> Fill Holes. Again, this is not a perfect assumption by the software, but because all previous manipulations are equal for each image in the experimental run I assumed equality of the fill hole algorithm across all the images. Once the T_{zero} image was sufficiently manipulated I then asked ImageJ to count the number of cells via the Analyze -> Analyze Particles menu. On the resulting pop-up window, I set the following parameters. For size I asked it to include anything from '20 – Infinity;' anything larger than 20 square pixels will be counted as one particle and anything smaller than 20 square pixels will be eliminated from the count. I left the circularity metric as is and checked the 'Display Results' box and also the 'Exclude Edges' box to exclude any partial cells on the edges of the image. Once ImageJ completed counting, it generated a pop-up window with the number of particles counted, see Figure 3C, and some metrics about each particle including area and an individual number. For the purposes of these experiments, I only recorded the number of particles. Once this analysis was done for the T_{zero} image in each run the masked image was left open for the remainder of the image manipulations for that particular experimental run.

To compare each subsequent image to the T_{zero} image, I opened each subsequent timepoint image in ImageJ and converted it to a binary mask using the steps described above, asked ImageJ to set the dividing borders and also fill any holes. Before counting, I subtracted the second timepoint in consideration from the original timepoint, T_{zero}, via the Process -> Image Calculator command in ImageJ. In the subsequent pop-up window, I always ensured that the T_{zero} image was in the Image 1 position and the timepoint in consideration was in the Image 2 position

and the ‘Operation’ was the ‘Subtract’ command. This algorithm generates a new image based on the pixel by pixel subtraction of the second image from the first image. I then used the previously described counting algorithm from above to analyze the differences in the two images. I recorded this particle count in the appropriate timepoint on a spreadsheet and calculated the percent difference ratio for each time point compared to T_{zero} within an experimental run.

Statistical analysis was done to compare cumulative separation events within each experimental run for a particular strain and also between the differing TBR1 and TBR5 strains. I used a single factor ANOVA to compare the experimental runs for the same strains and then used an F-test to determine variance between the average percent difference ratios for the TBR1 & TBR5 strains. Based on the outcomes of the F-test, I then used a T-test for two samples using equal or unequal variances.

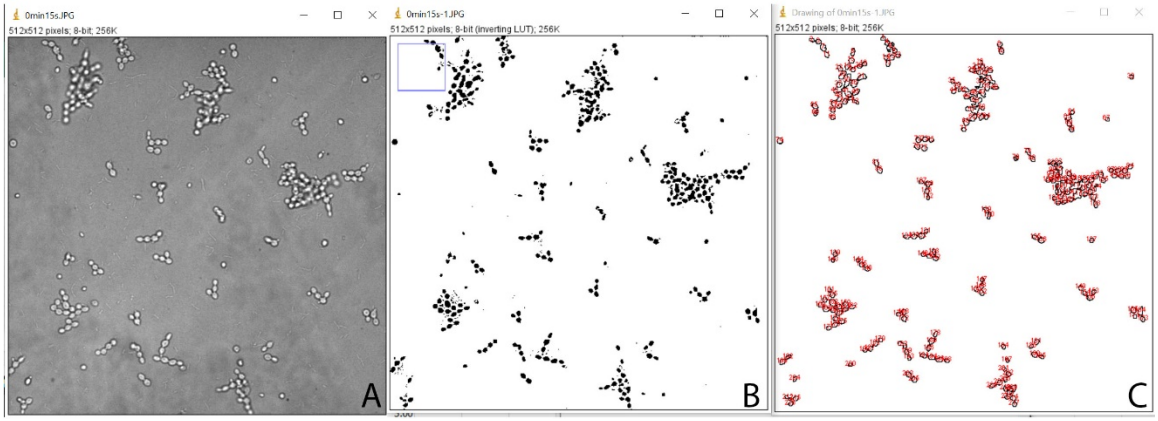

Figure 3. Image Analysis. Image 3A is the Jpeg exported from the microscope capture software. Image 3B is the binary image generated in ImageJ. Image 3C is a representation of the individually counted particles from ImageJ.

CHAPTER IV

RESULTS

I was able to successfully develop a PDMS flow chamber to analyze the separation events of the wildtype strain, SK1 *Saccharomyces cerevisiae* outlined in Aim 1.a. I tried several prototypes with varying levels of success and reached a simple, yet functional design that yielded the best results in terms of visualization of the separation events and allowing an unobstructed laminar flow through the chamber. The final design, as seen in Figure 4, with the 18-gauge wire throughout the entire length of the chamber, allowed us to adequately visualize the yeast adhered to the plain glass substrate, count the specific separation events and develop a separation profile for the SK1 strain of yeast.

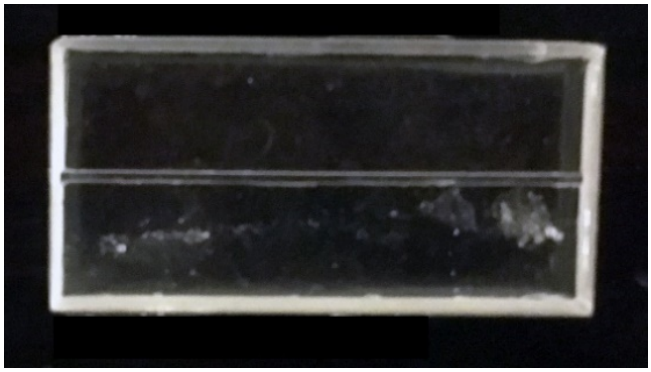

Figure 4. Final Prototype of the Flow Chamber. The final prototype of the flow chamber made out of PDMS. The middle channel is where image analysis occurs and where the PBS is pushed through the chamber by the peristaltic pump.

Figure 5 clearly elucidates the goals outlined in Aim 1.b. I successfully developed a flow chamber that demonstrates an adequate method of visualization and imaging of the yeast adhered to the surface of the flow chamber. The T_{zero} image, Figure 5A, is the image that I made a binary mask of and subtracted each subsequent timepoint image from. Images represented by Figures 5B – 5I are the images taken at the even minutes of the eight-minute experimental run. The flow rate profile is noted in the top right corner of the montage and indicated on each image. The group of seven cells to the right of the black arrow remained in place and in the same orientation with one another through minute three, Figure 5D. At minute four, Figure 5E, five of the cells have separated from the group of two immediately below it. By minute five, Figure 5F, they have changed orientation once again and remained in that orientation through minute eight, Figure 5I. The cells to the left of the asterisk changed orientation slightly at the one-minute timepoint, Figure 5B. By the two-minute timepoint, Figure 5C, they changed orientation slightly again but retained this orientation throughout the remainder of the experimental run.

At the five-minute timepoint, Figure 5F, a large group of unadhered cells moved into the field of view in the top left corner. They moved slightly further into the field of view at the six-minute timepoint, Figure 5G, but never seemed to fully pass through the entire field of view as they were still visible at the eight-minute timepoint, Figure 5I.

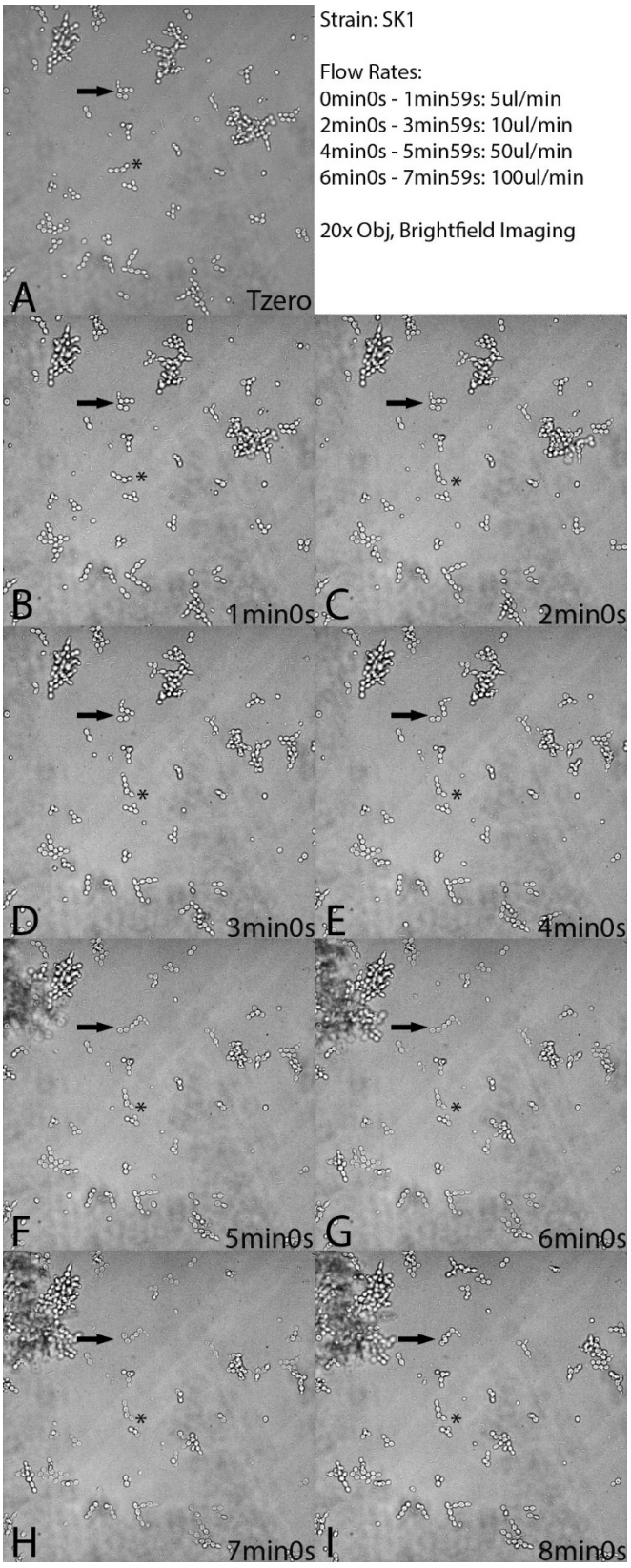

Figure 5. Image Montage of SK1 Experimental Run.

An image montage of the images from the even minutes of an experimental run of the SK1 strain of wildtype Saccharomyces cerevisiae. The black arrow indicates the group of 7 cells directly to the right of the arrow and tracks their position throughout each image. The asterisk indicates the group of 4 cells directly to the left of the asterisk.

I analyzed three different experimental runs of the SK1 strain of wildtype *Saccharomyces cerevisiae* through the flow chamber. For each time point I recorded the particle count of the image created by subtracting the image from each timepoint from the T_{zero} image; afterwards I calculated a percent difference between the subtraction counts and the original T_{zero} counts. I then plotted the percent difference ratio values with the average calculated ratio between the timepoints against the established flow rate profile in Figure 6. The standard deviation is represented by the error bars on the average data. Overall the data gathered within one standard deviation from the trendline with the exception of a few outliers. The separation events profile in Figure 6 also demonstrates that the flow rate can affect an increase in separation events as timepoints progress of the wildtype SK1 *Saccharomyces cerevisiae* strain, meeting the goals in Aim 1.c.

To determine statistical significance and compare the three runs to one another I did a single factor ANOVA in MS Excel represented in Figure 7. The *p-value* is greater than 0.05 indicating that the data are not statistically significant and is appropriate to group them together; I assumed the average values represent an accurate separation profile.

To examine the goals in Aim 2, I also established separation profiles for three experimental runs of the percent difference ratios in events for the TBR5, Flo11p knockout, strain of *Saccharomyces cerevisiae* through the flow chamber using the same previously described protocols for the SK1 strain. I then plotted the percent difference ratios with the average calculated ratios between the timepoints against the established flow rate profile in Figure 8. As the percent difference ratios approach the zero axis, the greater the difference in cell number and deviation from the T_{zero} timepoint. The standard deviation is represented by the error bars on the average data. The data are not tightly grouped for the TBR5 strain and there is one whole experimental run that lies on the border of the upper standard deviation calculation from the

average. The first half of a different experimental run lie on the borders of the lower standard deviations from the average.

To determine statistical significance and compare the three runs to one another I did a single factor ANOVA in MS Excel represented in Figure 9. The *p-value* is less than 0.05 indicating that the data are statistically significant and it is not appropriate to group them together; therefore, the average values do not represent an accurate separation profile. If I remove the outlying experimental run (Run 3) from the data, the graph changes drastically as seen in Figure 10. The data are now more tightly packed and fall within one standard deviation of the average. This is a more accurate approximation of the TBR5 strain separation profile.

To determine if the new approximation is statistically significant and compare the two runs to one another I ran an F-test to determine equal or unequal variances represented in Figure 11a. The resulting *F value* of the F-test was higher than the F-critical value meaning that the two runs had unequal variances. I then ran a t-test: Two Sample Assuming Unequal Variances test represented in Figure 11b. The resulting *p value* was greater than 0.05 indicating that these two groups are not statistically different and is appropriate to group them together proving that our exclusion of the outlying run was beneficial for our analysis and achieving the goals set forth in Aim 1.a.

To further examine the goals in Aim 2, I also established separation profiles for three experimental runs of the wildtype TBR1 strain of *Saccharomyces cerevisiae* through the flow chamber using the same previously described protocols for the SK1 strain. I then plotted the percent difference ratios with the average calculated ratios between the timepoints against the established flow rate profile in Figure 12. The standard deviation is represented by the error bars on the average data. The data here are rather problematic. Again, there is one experimental run

completely outside the standard deviation which requires further manipulation similar to the processes done for the TBR5 strain.

If Run3 is again removed from consideration in the data series, the graph of the separation profile changes in Figure 14. The beginning of the data is problematic but seems to fall in line with the data from the other series around the sixth timepoint. Based on the Single Factor ANOVA in Figure 13, with a reported *p value* less than 0.05, the data are statistically significant from one another and thus should not be grouped together.

Looking at the results of the F-test to test for equal or unequal variances in Figure 15a, the *F value* is lower than the *F critical value* indicating equal variances. Based on the results of the F–test in Figure 15a, I then ran a t-Test: Two Sample Assuming Equal Variances test represented in Figure 15b and the resulting *p-value* indicates that the data are not statistically significant and I can group these two runs together as an approximation for an accurate separation for TBR1. With this successful approximation of a separation profile for the TBR5 wildtype strain, I achieved the goals set forth in Aim 2b.

With separation profiles for both the TBR5 and TBR1 strains I can now compare the two profiles. I graphed the average of each approximation of the separation profile (See Figures 10 and 14.) based on the changes I made to the data in Aims 2.a. and 2.b in Figure 16. The TBR5 strain has error bars of one standard deviation of the two average percent difference ratios of each data series represented in this graph. The trendline is based off the TBR5 average data series.

To determine statistical significance between the two strains, I did an F-test to determine equal or unequal variances and the comparison of the *F-value* to the *F-critical value* denotes equal variance between the two groups of data. I then completed a t-Test: Two Samples

Assuming Equal Variance and the reported *p value* was less than 0.05 which is indicative of a statistical difference between the data sets for the two strains of *Saccharomyces cerevisiae.*

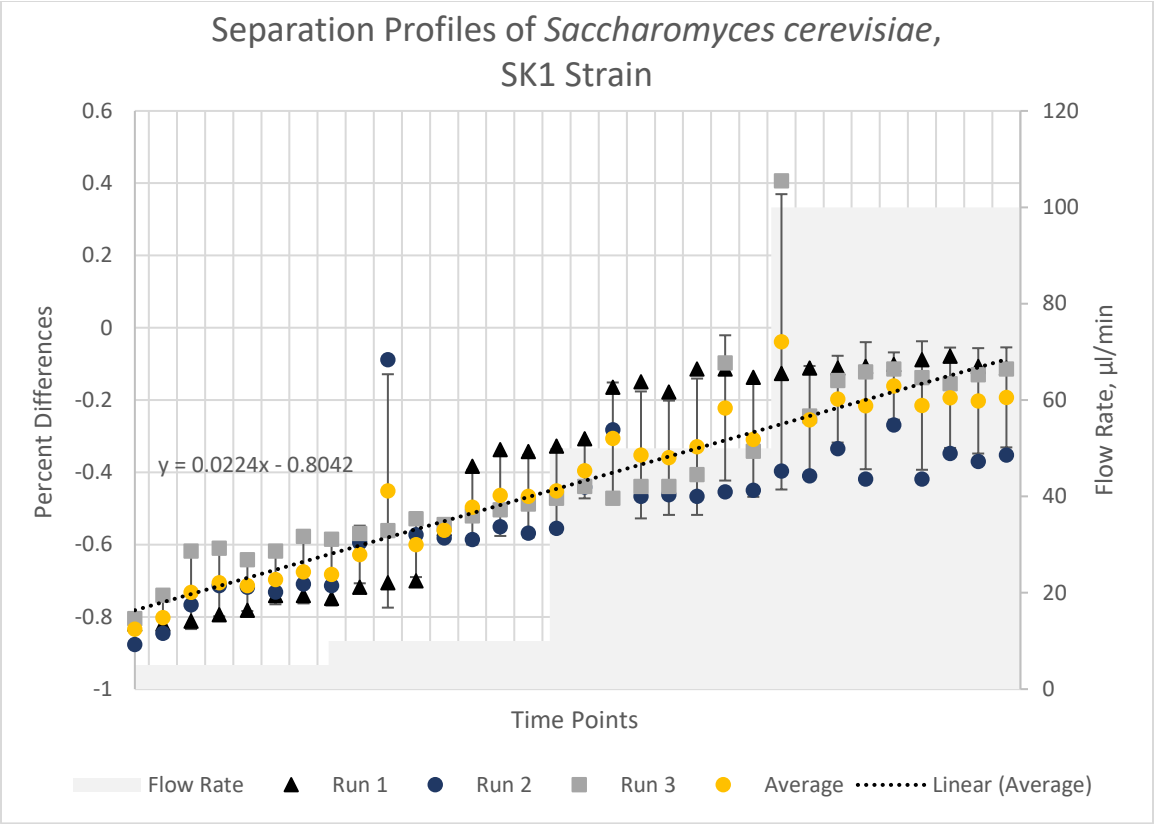

Figure 6. Separation Profiles of Saccharomyces cerevisiae, SK1 Strain. Calculated percent difference ratios of the number of particles between T_{zero} and the subsequent time points for 3 experimental runs of the SK1 wildtype strain. Average is represented by yellow circles and trendline. Plotted against established flow rate protocol.

ANOVA: Single Factor

SUMMARY – SK1

Groups	*Count*	*Sum*	*Average*	*Variance*
Run 1, SK1	32	-12.4391	-0.38872	0.086762
Run 2, SK1	32	-16.511	-0.51597	0.032346
Run 3, SK1	32	-12.7724	-0.39914	0.063208

ANOVA

Source of Variation	*SS*	*Df*	*MS*	*F*	*P-value*	*F crit*
Between Groups	0.319471	2	0.159735	2.62843	0.07755	3.094337
Within Groups	5.651812	93	0.060772			
Total	5.971283	95				

Figure 7. Single Factor ANOVA Results from the Three Experimental SK1 Runs Through the Flow Chamber.

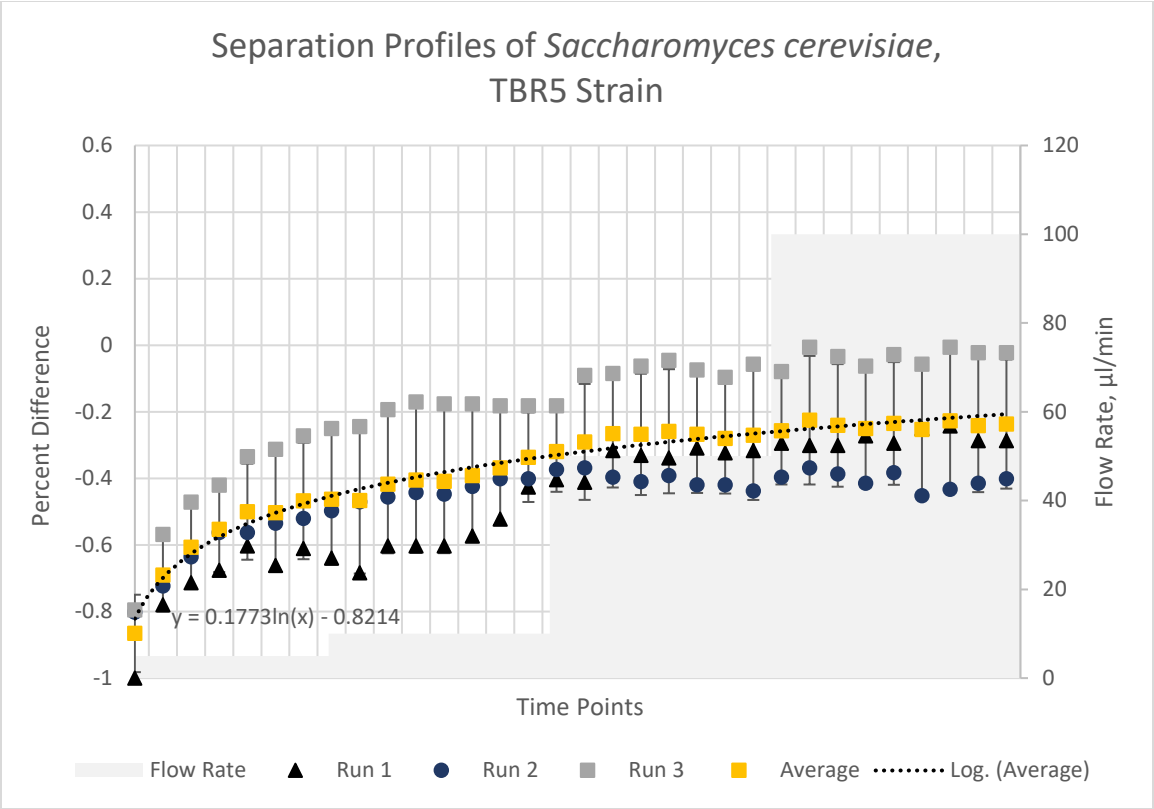

Figure 8. Separation Profiles of Saccharomyces cerevisiae, TBR5 Strain. Calculated Percent Differences of the number of particles between T_{zero} and the subsequent time points for 3 experimental runs of the TBR5 Flo11 Knockout strain. Average is represented by yellow circles and trendline. Plotted against established flow rate protocol.

ANOVA: Single Factor

SUMMARY TBR5

Groups	*Count*	*Sum*	*Average*	*Variance*
Run 1, TBR5	32	-14.9779	-0.46806	0.037405
Run 2, TBR5	32	-14.7465	-0.46083	0.010343
Run 3, TBR5	32	-5.76136	-0.18004	0.032507

ANOVA

Source of Variation	*SS*	*Df*	*MS*	*F*	*P-value*	*F crit*
Between Groups	1.726378	2	0.863189	32.26683	2.27E-11	3.094337
Within Groups	2.487898	93	0.026752			
Total	4.214277	95				

Figure 9. Single Factor ANOVA Results from the Three Experimental TBR5 Runs Through the Flow Chamber.

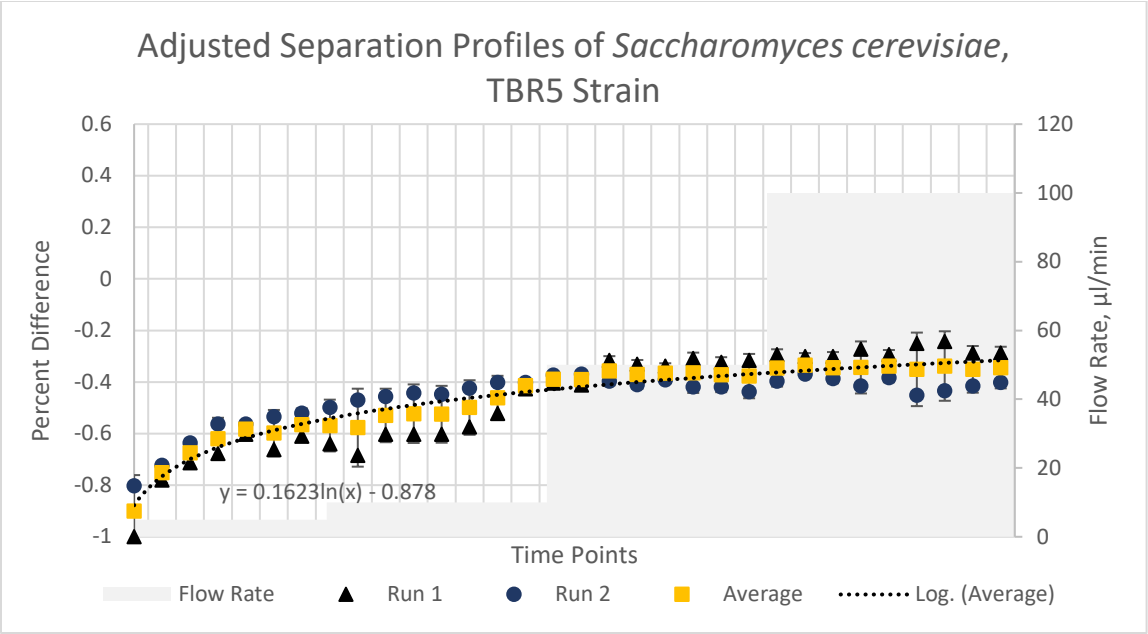

Figure 10. Adjusted Separation Profiles of Saccharomyces cerevisiae, TBR5 Strain. Calculated Percent Differences of the number of particles between T_{zero} and the subsequent time points for 2 experimental runs of the TBR5 Flo11 Knockout strain. Average is represented by yellow squares and trendline. Plotted against established flow rate protocol.

F-Test		
	Run 1	*Run 2*
Mean	-0.46806	-0.46083
Variance	0.037405	0.010343
Observations	32	32
Df	31	31
F	3.616539	
P(F<=f) one-tail	0.000292	
F Critical one-tail	1.822132	

11a

t-Test: Two-Sample Assuming Unequal Variances		
	Run 1	*Run 2*
Mean	-0.46806	-0.46083
Variance	0.037405	0.010343
Observations	32	32
Hypothesized Mean Difference	0	
Df	47	
t Stat	-0.1872	
P(T<=t) one-tail	0.426155	
t Critical one-tail	1.677927	
P(T<=t) two-tail	0.85231	
t Critical two-tail	2.011741	

11b

Figure 11. F-test (11a) and t-Test: Two Sample Assuming Unequal Variances (11b) for 2 Experimental Runs of the TBR5 Strain.

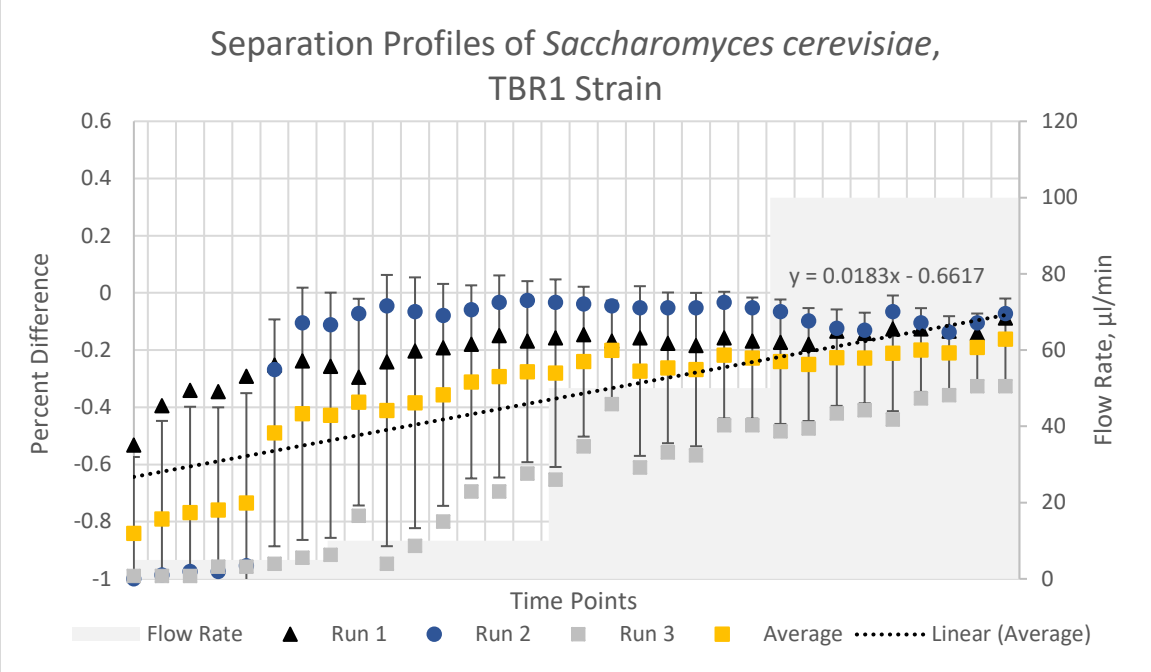

Figure 12. Separation Profiles of Saccharomyces cerevisiae, TBR1 Strain. Calculated Percent Differences of the number of particles between T_{zero} and the subsequent time points for 3 experimental runs of the TBR1 wildtype strain. Average is represented by yellow squares and trendline. Plotted against established flow rate protocol.

ANOVA: Single Factor

SUMMARY-
TBR1

Groups	*Sum*	*Average*	*Variance*
Run 1	-14.9779	-0.46806	0.037405
Run 2	-14.7465	-0.46083	0.010343
Run 3	-5.76136	-0.18004	0.032507

ANOVA

Source of Variation	*Df*	*MS*	*F*	*P-value*	*F crit*
Between Groups	2	0.863189	32.26683	2.27E-11	3.094337
Within Groups	93	0.026752			
Total	95				

Figure 13. Single Factor ANOVA Results from the Three Experimental TBR1 Runs Through the Flow Chamber.

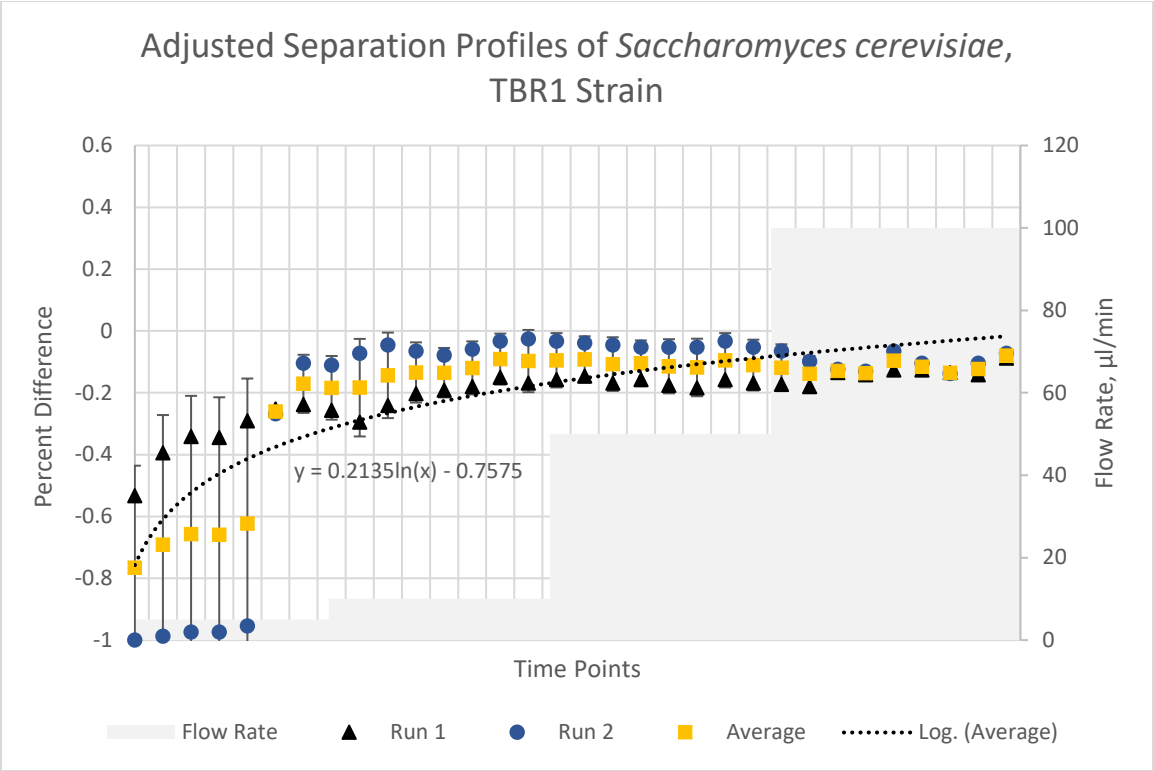

Figure 14. Adjusted Separation Profiles of Saccharomyces cerevisiae, TBR1 Strain. Calculated Percent Differences of the number of particles between T_{zero} and the subsequent time points for 2 experimental runs of the TBR1 wildtype strain. Average is represented by yellow squares and trendline. Plotted against established flow rate protocol.

F-Test		
	Run 1	*Run 2*
Mean	-0.2075	-0.21916
Variance	0.008687	0.112118
Observations	32	32
Df	31	31
F	0.077478	
P(F<=f) one-tail	1.06E-10	
F Critical one-tail	0.548808	

15a

t-Test: Two-Sample Assuming Equal Variances		
	Run 1	*Run2*
Mean	-0.2075	-0.21916
Variance	0.008687	0.112118
Observations	32	32
Pooled Variance	0.060403	
Hypothesized Mean Difference	0	
Df	62	
t Stat	0.189825	
P(T<=t) one-tail	0.425033	
t Critical one-tail	1.669804	
P(T<=t) two-tail	0.850066	
t Critical two-tail	1.998972	

15b

Figure 15. F-test (15a) and t-Test: Two Sample Assuming Equal Variances (15b) for 2 Experimental Runs of the TBR1 Strain.

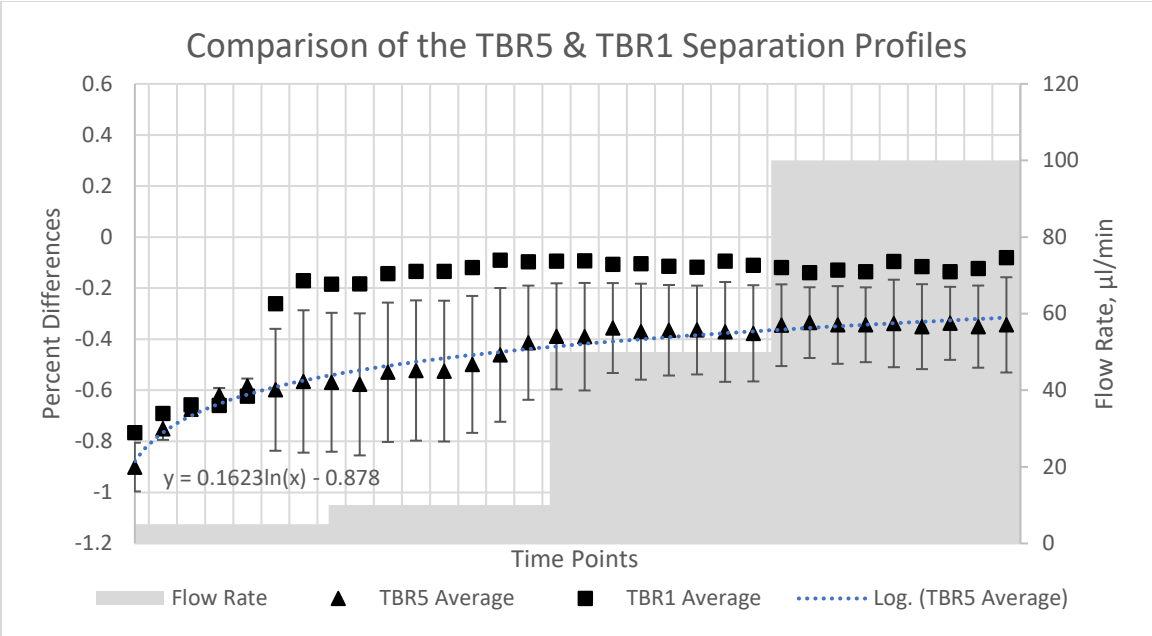

Figure 16. Comparison of the TBR5 & TBR1 Separation Profiles. Standard deviation is represented as plus and minus error bars on the TBR5 data series. Trendline is based off of the TBR5 data

F-Test		
	TBR5	*TBR1*
Mean	-0.46445	-0.21333
Variance	0.020066	0.043087
Observations	32	32
df	31	31
F	0.465712	
P(F<=f) one-tail	0.018505	
F Critical one-tail	0.548808	

17a

t-Test: Two-Sample Assuming Equal Variances		
	TBR5	*TBR1*
Mean	-0.46445	-0.21333
Variance	0.020066	0.043087
Observations	32	32
Pooled Variance	0.031576	
Hypothesized Mean Difference	0	
df	62	
t Stat	-5.65272	
P(T<=t) one-tail	2.13E-07	
t Critical one-tail	1.669804	
P(T<=t) two-tail	4.26E-07	
t Critical two-tail	1.998972	

17b

Figure 17. F-test (17a) and t-Test: Two Sample Assuming Unequal Variances (17b) for 2 Experimental Runs of the Average Percent Differences. This is a comparison of the average percent differences (approximated Separation Profiles) of the TBR5, Flo11p Knockout, and the TBR1, wildtype, strains.

CHAPTER V

DISCUSSION

I tested several different prototypes of our PDMS flow chamber before finding the final version with the square 18-gauge wire throughout the entire length of the flow chamber was the best design. After discovering that the size of the flow chamber itself would be a limiting factor in our ability to 3D print a chamber, I then sought out easily manipulatable materials that I could test several different designs with and after some literary searches I found that many labs are using PDMS to build flow chambers to their specific design specifications (Kang, 2017) (Marki, 2016) (Schmid, 2012) (Shrirao, 2010). The first prototypes of our flow chamber included ports for tubing from above the chamber. While this design seemed adequate to establish a laminar flow within the channel, it often caused leakage around the ports and sometimes the force of the flow rate from the pump caused excess liquid to pool under the chamber and subsequently lift the chamber off the cover glass whereupon it would float away. I then switched the ports to be level with the flow imaging channel. This prevented the leakage and pooling problems and allowed more precise control of the flow rate within the channel. Our next problem came with the visualization of the field of the imaging channel on the coverslip. During the making of the mold I had been previously using an 18-gauge round wire or capillary tube to make the imaging channel. This unfortunately limited the field of view immensely as the area of the capillary tube or wire that came into contact with the glass surface to too small an area. I then switched to a square 18-gauge wire which afforded us a greater field of view and allowed adequate visualization.

While the square geometry of the channel most probably creates eddies at the fringes and corners of the imaging channel I thought that the ease of visualization was of greater concern than the increased turbulence experienced by the cells. In fact, the increased turbulence is probably more indicative of a natural anatomical experience in the urethra. The urethra is not a perfect cylindrical space by any means (Garner, 2006) (Standring, 2008) and catheters are made of materials that are intended to bend and flex to accommodate the natural anatomy of the patient (Siddiq, 2012) (Wein, 2016). I acknowledge that the square geometry does present some issues in approximating the laminar flow and shear force and hope to approximate those adequately. Present studies are trying to improve the geometry of the imaging channel with a wire or impression that is a semi-circular shape, flat where it comes into contact with the glass and circular in the remaining volume of the channel to establish a less perturbed laminar flow.

Figure 5 is an image montage of one experimental run with the SK1 wildtype yeast, *Saccharomyces cerevisiae*; a full montage of all the images in that run can be found in the appendix (Supplemental Figure 1). Firstly, it is a demonstration that our flow chamber design was successful, meeting the goals presented in Aim 1.a and Aim 1.b. We can clearly visualize and image the yeast adhered to the coverslip and subsequently use that image to count the number of particles present for analysis. Secondly it demonstrates that the changing flow rate in the chamber does affect the adhesion of the wildtype yeast in the field of view. We have already learned that *S. cerevisiae* uses the Flo1p1 protein in its cell wall to adhere to latent surface through a hydrophobic domain in its N terminus (Reynolds, 2001) (Kraushaar, 2015). I established our flow rate profile and specific rates based on previous trials of several different flow rate profiles and rates (data not reported). I found that after an initial response to the initiation of the flow rate, the same constant rate over the same time period produced little to no response from the cells. Establishing a step-up profile allowed us to adequately visualize

responses from the cells to the changing flow rates and quite possibly gave them time to adapt and cluster more Flo11p to specific areas on their surface. Unfortunately, we have no way to determine if that is indeed the case but future studies should endeavor to fluorescently label the Flo11 and track its progress over the surface of the cell with increasing flow rates to test its response to increasing shear forces.

Once the design of our flow chamber was confirmed I then moved to confirm our flow rate profile selection by analyzing separation events in a wildtype yeast, SK1. Using specific image analysis techniques, I was able to count the differences in particles between different timepoints collected under different flow rates and compare those to the original, T_{zero} timepoint, where there was no active flow rate. Once I obtained those data, I then compared them to one another and using statistical analysis were able to establish a separation profile for the SK1 yeast as seen in Figure 6.

As the percent difference ratio data approaches zero it is indicative of greater change between the timepoint in question and the T_{zero} timepoint, from which we can draw a direct correlation to increased separation events. While percent difference ratios are plotted it is important to remember that these data represent a discreet number of particles that are different from the T_{zero} timepoint. The algorithm ImageJ uses to subtract an image from the T_{zero} timepoint will always use the T_{zero} image as reference, thus each subtraction and particle count will never exceed the initial T_{zero} particle count. If there were no separation events, the subsequent time point images would have a percent difference ratio of 1, if the images were completely different there would be a percent difference ratio of 0. I chose not to represent the data solely in particle numbers because our system is not a closed system; cells from upstream in the flow chamber can move into the field of view and the cells within the field of view can move out, thus demonstrating the need to report percent difference ratios. Correlating the percent difference

ratios to separation events we find that as the flow rate increases there are increased separation events but the separation events follow a linear trendline and increase linearly instead of exponentially similar to the flow rates. While I was able to meet the goals outlined in Aim 1.c I cannot make any statements about the role that Flo11p plays in this observed separation event profile other than to assume that Flo11p is indeed responsible for the adhesion of the wildtype yeast to the plain glass substrate. On average 80% of the SK1 cells were no longer adhered to the surface of the plain glass by the end of the experiments after 8 minutes. I can posit that the shear forces were able to overwhelm the physical adhesive properties of the Flo11p protein in 80% of the cells.

While our experiments cannot evaluate the actual cellular response of Flo11p to the increasing shear forces, I can confirm and mete the role shear forces play in overcoming the Flo11p adhesive properties in separation events by comparing a yeast strain that can translate functional copies of Flo11p, TBR1, to a yeast strain that has had the Flo11 gene knocked out so there should be no functional copies of Flo11p present.

To calculate shear force (Figure 18), I used the equation from Nejadnik.

$\tau = F/A = \eta\sigma$, where η is the shear stress, F the force, A the area on which the force is exerted, η the absolute viscosity and σ the shear rate. σ can then be defined as:

$\sigma = 3Q/2b^2 * w$, where Q is the flow rate, b being the half depth of the chamber system and w being the width. I assumed a viscosity of 1 for the PBS. Since the 18g wire is square, w is 1.02mm and b is 0.51mm.

Examining figures 10 and 14 we can see the established separation profiles for the TBR5, *flo11Δ,* strain and the wildtype TBR1 strains, meeting the goals of Aims 2.a and 2.b. Both of these profiles fit a logarithmic trendline in separation events in response to the increasing flow

rates. The separation events for both of these strains of yeast seem to respond more quickly to the initiation of the flow rate and the early time points but then gradually level off and have a lesser magnitude of change in separation events in response to the continued increasing flow rates. Figure 16 directly compares the average separation profiles for the two strains to one another, meeting the goals in Aim 2.c. The TBR5 strain has fewer separation events than the TBR1 strain. The TBR1 strain has almost 100% change in particle numbers by the end of the separation profile meaning that the shear forces almost completely overwhelm the adhesive properties of the Flo11p protein in these cells. In stark contrast, the TBR5 strain only has a 60% change in particle numbers and retains around 40% of the original particles at the end of the experiments. Our hypothesis stated that I expected that the TBR5 strain would have increased separation events because of the lack of a functional Flo11p protein, yet our data does not support that supposition at all. Since the open reading frame for the *flo11* gene has been completely replaced, it would not have any portion of the protein present in the cell wall surface. Obviously, the cells were able to adhere to surface of the glass coverslip without the Flo11p protein. Both of the TBR strains do express other forms of the Flo proteins which are involved in cell-cell adhesion (Vachova, 2011) (Reynolds, 2001). There is also some evidence to suggest that some microbes actually have increased adhesion or conversely, decreased separation events, as shear stress increases (Lecuyer, 2011). Could the TBR5, *flo11Δ,* strain of yeast be accommodating the increases in shear force stresses on the cells and changing the type of bonds adhering to the surface? Lecuyer posits that *E.coli* and *P. aeruginosa* facilitate stronger adhesions to surfaces with catch bonds (Lecuyer, 2011), but do we find these same type of catch bonds in the fungal adhesins? Chan and Lipke found that increasing shear stress does increase resident adhesion time of *S. cerevisiae* and the initiation of catch bonds similar to bacterial models (Chan, 2014). I posit that although we would expect a *flo11Δ* strain to have increased separation events, the fact that my data supports the

opposite supposition is due to the catch bond formation and aggregation of the remaining Flo adhesins on the surface of the yeast cell wall. Quite simply, the increased stress on the TBR5 strain due to the lack of the Flo11p protein and increasing shear force causes a greater response in magnitude from the adhered cells

While our data do not support our initial posited hypothesis, based on literature findings I can suppose an alternative explanation that supports the data found. While this was initially surprising, we find that that the creation of the catch bonds is supportive of our data and a reasonable alternative hypothesis. Both the TBR strains separation event profiles seem to level off after an initial response to the initiation of the flow rate indicating some change in response to increased shear stress. For future studies we'd like to do more FIB-SEM experiments to visualize these catch bonds both on latent surfaces and the engineered nano-structured surfaces that our lab has developed (Nowlin, 2015). Understanding and visualizing these initial steps of deposition and adhesion of fungal microbes to latent surfaces is vital to our laboratory's attempts to develop commercially available microbicidal nanostructured surfaces for medical in-dwellings and catheters.

Calculated Shear Force			
Q, Flow Rate	**σ, Shear Rate**	**η, viscosity**	**τ, Shear Force**
5 ul/min	29.4	1	29.4
10 ul/min	58.8	1	58.8
50 ul/min	294.1	1	294.1
100 ul/min	588.2	1	588.2

Figure 18. Calculated Shear Force

REFERENCES

Aguilar-Uscanga, B. a. (2003). A Study of the Yeast Cell Wall Composition and Structure in Response to Growth Conditions and Mode of Cultivation. *Letters in Applied Microbiology, 37*(3), 268 - 274.

Busscher, H. J. (2006, Jan). Microbial Adhesion in Flow Displacement Systems. *Clinical Microbiology Reviews, 19*, 127-141.

Chan, C. X. (2014). Role of Force-Sensitive Amyloid-Like Interactions in Fungal Catch Bonding and Biofilms. *Eukaryotic Cell, 13*(9), 1136 - 1142.

Douglas, L. M. (2007). Expression and Characterization of the Flocculin Flo11/Muc1, a Saccharomyces cerevisiae Mannoprotein with Homotypic Properties of Adhesion. *Eukaryotic Cell, 6*(12), 2214 - 2221.

Farrag, H. A.-D.-S.-L. (2015). Microbial Colonization of Irradiated Pathogenic Yeast to Catheter Surfaces: Relationship Between Adherence, Cell Surface Hydrophobicity, Biofilm Formation, and Antifungal Susceptibility. A Scanning Electron Microscope Analysis. *International Journal of Radiation Biology, 91*(6), 519 - 527.

Garner, L. P. (2006). *Color Atlas of Histology* (4th ed.). Baltimore: Lippincott Williams & Williams.

Garret, T. R. (2008). Bacterial Adhesion and Biofilms on Surfaces. *Progress in Natural Science, 18*, 1049 - 1056.

Hermansson, M. (1999). The DLVO Theory in Microbial Adhesion. *Colloids and Surfaces B: Biointerfaces., 14*, 105 - 119.

Hooton, T. M. (2010). Diagnosis, Prevention, and Treatment of CatheterAssociated Urinary Tract Infection in Adults: 2009 International Clinical Practice Guidelines from the Infectious Diseases Society of America. *Clinical Infectious Diseases, 50*, 625 - 663.

Ivanova, E. P. (2012). Natural Bactericidial Surfaces: Mechanical Rupture of Pseudomonas aeruginosa Cells by Cicada Wings. *Small, 8*(16), 2489 - 2494.

Ivanova, E. P. (2013). Bactericidal Activity of Black Silicon. *Nature Communications, 4*, 2838.

Kang, M. B. (2017). Fabrication of Functional 3D Multi-Level Microstructures on Transparent Substrates by One Step Back-Side UV Photolithography. *RSC Advances, 7*, 13353-13361.

Kollar, R. R. (1997). Architecture of the Yeast Cell Wall, b(136)-Glucan Interconnects Mannoprotein, b(133)-Glucan, and Chitin. *The Journal of Biological Chemistry, 272*(28), 17762 - 17775.

Kraushaar, T. B.-U. (2015). Interactions by the Fungal Flo11 Adhesin Depend on a Fibronectin Type III-like Adhesin Domain Girdled by Aromatic Bands. *Structure, 23*(6), 1005 - 1017.

Lecuyer, S. R. (2011). Shear Stress Increases the Residence Time of Adhesion of Pseudomonas aeruginosa. *Biophysical Journal, 100*, 341 - 350.

Levin, D. E. (2011). Regulation of Cell Wall Biogenesis in Saccharomyces cerevisiae: The Cell Wall Integrity Signaling Pathway. *Genetics, 189*, 1145 - 1175.

Marki, A. G. (2016). Microfluidics-Based Side View Flow Chamber Reveals Tether-to-Sling Transition in Rolling Neutrophils. *Scientific Reports, 6*, 28870.

Mohammadi, P. S. (2012). Isolation and Detection of Yeast Biofilms From Urine Catheters of Infectious Patients. *Jundishapur Journal of Microbiology, 5*(4), 533 - 536.

Nathan, C. (2015). From Transient Infection to Chronic Disease: Can Some Infections "Scar" the Immune System? *Science, 350*(6257), 161.

Nejadnik, M. R. (2008.). Determination of the Shear Force at the Balance Between Bacterial Attachment and Detachment in Weak-Adherence Systems, Using a Flow Displacement Chamber. *Applied and Environmental Microbiology., 74*(3), 916 - 919.

Nowlin, K. B. (2015). Adhesion-Dependent Rupturing of Saccharomyces cerevisiae on Biological Antimicrobial Nanostructured Surfaces. *J. R. Soc. Interface, 12*, 20140999.

Pogodin, S. H. (2013). Biophysical Model of Bacterial Cell Interactions with Nanopatterned Cicada Wing Surfaces. *Biophyscial Journal, 104*, 835 - 840.

Ramsook, C. B. (2010). Yeast Cell Adhesion Molecules Have Functional Amyloid-Forming Sequences. *Eukaryotic Cell, 9*(3), 393 - 404.

Reynolds, T. B. (2001). Baker's Yeast, a Model for Fungal Biofilm Formation. *Science, 291*, 878 - 881.

Schmid, L. W. (2012). Novel Surface Acoustic Wave (SAW)-Driven Closed PDMS Flow Chamber. *Microfluid Nanofluid, 12*, 229-235.

Shrirao, A. B.-C. (2010). *Microfluidics Labs Using Devices Fabricated by Soft-Lithographic Replication of Scotch Tape Molds.* New Jersey Institute of Technology, Department of Electrical and Computer Engineering, Newark, NJ.

Siddiq, D. M. (2012). New Strategies to Prevent Catheter-Associated Urinary Tract Infections. *Nature Reviews, Urology, 9*(6), 305 - 314.

Standring, S. a. (2008). *Gray's Anatomy: The Anatomical Basis of Clinical Practice.* Edinburgh.: Churchill Livingstone/Elsevier.

Tailly, T. a. (2016). Fundamentals of Urinary Tract Drainage. In A. J. Wein, *Campbell-Walsh Urology* (pp. 119 - 135). Philadelphia: Elsevier.

Vachova, L. S. (2011). Flo11p, Drug Efflux Pumps, and the Extracellular Matrix Cooperate to Form Biofilm Yeast Colonies. *The Journal of Cell Biology., 194*(5), 679 - 687.

Wein, A. J. (2016). *Campbell-Walsh Urology.* Philadelphia: Elsevier.

Young, K. D. (2006). The Selective Value of Bacterial Shape. *Microbiology and Molecular Biology Reviews., 70*(3), 660-703.

APPENDIX A

MATERIALS

Dow Corning Sylgard 184 Silicone Elastomer (PDMS)

3D Printed Shell

18 Gauge square wire

Ted Pella Large, 3x3.5 inch Cover Slips

Harvard Apparatus Peristaltic Pump 11 Elite Series and tubing

TBR5, and TBR1 Strains of *Saccharomyces cerevisiae*

Zeiss Axio Spinning Disc Confocal Fluorescence Microscope with Live Cell Imaging

APPENDIX B

SUPPLEMENTAL FIGURES

Supplemental Figure 1. Image Montage of SK1 Experimental Run. Image montage of images from experimental run of SK1 strain through experimental chamber. One image is taken every 15 seconds from 0min0s and the initiation of the flow rate. The flow rate is the established flow rate profile discussed in the methods section.

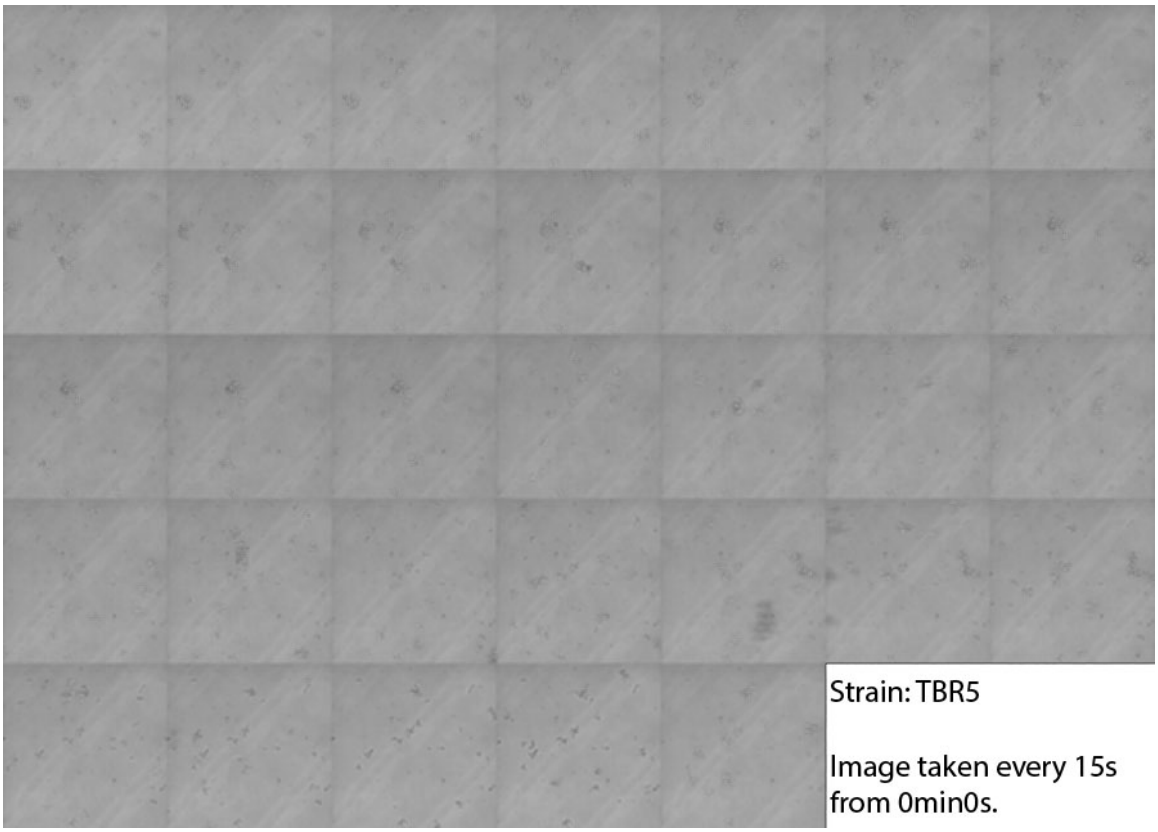

Supplemental Figure 2. Image Montage of TBR5 Experimental Run. Image montage of images from experimental run of TBR5 strain through experimental chamber. One image is taken every 15 seconds from 0min0s and the initiation of the flow rate. The flow rate is the established flow rate profile discussed in the methods section.

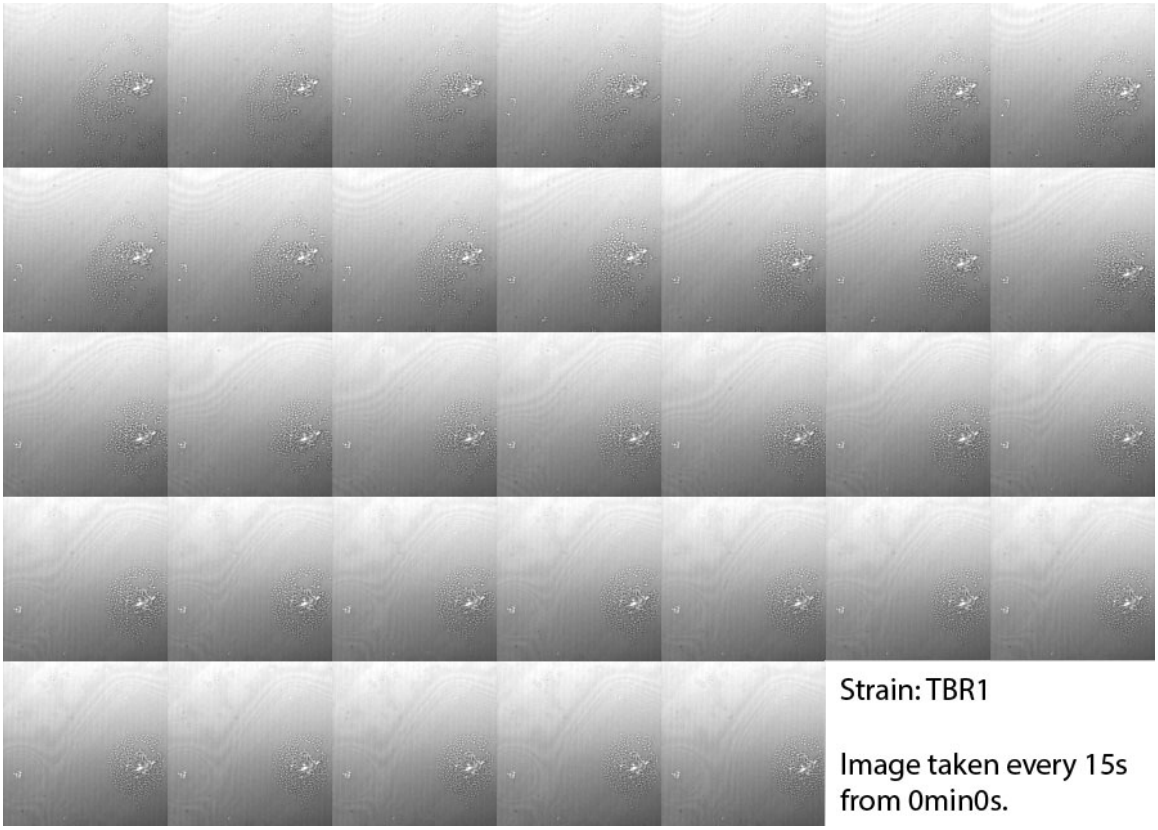

Supplemental Figure 3. Image Montage of TBR1 Experimental Run. Image montage of images from experimental run of TBR1 strain through experimental chamber. One image is taken every 15 seconds from 0min0s and the initiation of the flow rate. The flow rate is the established flow rate profile discussed in the methods section.